metals

MDPI

Article

Effects of C and Nb on Pore-Grain Boundary Separation Behavior during Sintering of 420 Stainless Steel

Tao Wen [1,2], Hao He [1,*], Jia Lou [2,*], Mengqi Gan [2], Xin Luo [2], Yuhang Huang [2] and Wei Xu [3]

[1] School of Microelectronics and Materials Engineering, Guangxi University of Science and Technology, Liuzhou 545006, China; 213301068@csu.edu.cn
[2] School of Materials Science and Engineering, Xiangtan University, Xiangtan 411105, China; 13762360059@163.com (M.G.); 202021001631@smail.xtu.edu.cn (X.L.); 202021001709@smail.xtu.edu.cn (Y.H.)
[3] The Key Lab of Guangdong for Modern Surface Engineering Technology, National Engineering Laboratory for Modern Materials Surface Engineering Technology, Institute of New Materials, Guangdong Academy of Sciences, Guangzhou 510650, China; xuw0907@163.com
* Correspondence: 100001865@gxust.edu.cn (H.H.); lou3166@xtu.edu.cn (J.L.)

Abstract: This study investigated the evolution of density, grain size, and pore characteristics during the sintering of metal injection molding (MIM) 420, 420 + 0.3C and pre-alloyed 420Nb stainless steel powders. The results show that C promotes the reduction of oxides on the surface of stainless steel, thereby accelerating sintering at 1330 °C, which is the initial sintering stage of MIM 420. MIM 420Nb showed the slowest sintering rate due to the strong binding force between Nb and C. At 1350 °C, the sintering densities of MIM 420 and 420 + 0.3C slightly improved, whereas their grain sizes grew significantly. Scanning electron microscopy images show grain boundary-pore separation, which significantly retarded the grain boundary diffusion mechanism and hence reduced the densification rate. The addition of C accelerated the pore-grain boundary separation; thus MIM 420 + 0.3C showed the lowest density at this temperature among the materials analyzed in this study. Nb suppressed the grain growth rate; thus, MIM 420Nb exhibited the highest density among the three materials. At 1370 °C, MIM 420 + 0.3C reached the highest density owing to the creation of a liquid phase. Theoretical calculations proved that there is a linear relationship between the grain boundary area per unit volume and the interfacial pore area per unit volume. Furthermore, when the ratio of grain size to pore size is 28, the contact probability between the grain boundaries and pores is significantly reduced to approximately 10%, leading to an extremely slow densification rate and a rapid grain growth rate, which is consistent with the experimental results.

Keywords: pore-grain boundary separation; sintering; metal injection molding; 420 stainless steel; density

Citation: Wen, T.; He, H.; Lou, J.; Gan, M.; Luo, X.; Huang, Y.; Xu, W. Effects of C and Nb on Pore-Grain Boundary Separation Behavior during Sintering of 420 Stainless Steel. *Metals* **2022**, *12*, 1186. https://doi.org/10.3390/met12071186

Academic Editor: Antonio Mateo

Received: 13 June 2022
Accepted: 8 July 2022
Published: 12 July 2022

1. Introduction

Type 420 stainless steel is a typical "blade-grade" martensitic stainless steel with a high hardness, strength, and wear resistance. It is widely used in cutting tools, turbine blades, and surgical/medical equipment [1,2]. However, its poor processing performance limits the further development of usage in complex shaped parts. Metal injection molding (MIM) allows the rapid large-scale production of metallic components with high geometrical complexities [3,4]. Extensive research is currently being conducted on the microstructure and mechanical properties of the MIM 420 stainless steel, to meet the requirement of high hardness parts with low cost.

However, 420 stainless steel currently faces certain fundamental issues, including sintering difficulties; therefore, the MIM industry is focusing more on 316 or 17-4PH stainless steel. Sintering at the relatively low temperature of 1300–1350 °C can barely achieve a high density. Sintering at higher temperatures fails to appreciably improve the density and leads to a significant increase in the grain size, which degrades the mechanical

properties. An et al. [5] found that when the sintered density of 420 stainless steel was 94%, the grain size reached 60 μm, and pore-grain boundary separation takes place; these effects were not observed in HK30 [6] or 316L [7]. This is because grain boundary diffusion is the main mechanism in the middle and later stages of sintering. The vacancies of pores in contact with grain boundaries can be eliminated by grain boundary diffusion. However, a very rapid grain growth reduces the possibility of the contact by causing holes to break away from the grain boundaries. The pore-grain boundary separation is a critical issue in the sintering of ceramics [8] and has also been reported in metals, such as Nb, Cu, and W [9–11]. In general, it occurs at a relative density of approximately 90% [9] and affects the subsequent sintering stages. Guo et al. [12] controlled the pore-grain boundary separation of $MgAl_2O_4$ through a pretreatment process. The density of the sample after sintering for 1 h increased from 94% to 98%, and the average grain size increased to 1.9 μm, which enhanced its hardness. To overcome the drawback of a low sintering density, some activation sintering methods, such as pressure sintering, are employed in the sintering of 420 stainless steel.

Studies have found that the addition of alloying elements effectively promotes densification [13–16] and has an important influence on the microstructure and mechanical properties [17]. The effects of adding non-metallic elements, such as C or B on MIM stainless steel, have been intensively investigated. Addition of C reduces the surface oxide concentration to promote sintering at low temperatures and decreases the liquidus of the material at high temperatures. Giménez et al. [18] found that the sintering window of T42 steel was enlarged from 5 °C to 10 °C by the addition of 0.4% graphite. Zhang et al. [19] and Harun et al. [20] found that the densities of HK30 and 440C increased significantly with an increase in the carbon content. However, it is uncertain that whether the sintering of 420 can be improved by adding carbon alone, because carbon promotes grain growth. Therefore, addition of strong carbide-forming elements, such as Nb, Cr, Mo, or Ti, has received particular attention. In the earlier research, alloying elements were mostly added in the powder form, which led to partial diffusion and Kirkendall holes in the matrix, thereby hindering the densification and homogenization of the alloy [21]. Recent studies have focused on adding the elements by means of pre-alloying. Zhang et al. [22] compared the effects of a mixed powder and fully pre-alloyed powder on the Ni-Mo-Cu alloy steel and found that the bending strength of the alloy steel using the fully pre-alloyed powder increased by 34%. Zhuang et al. [23] studied a 440C stainless steel pre-alloyed with 1.5 wt.% Nb and found that the sintering window was increased from 10 °C to 30–50 °C. Using Nb for sintering is a possible solution to the sintering difficulties of 420 stainless steel because it is a strong carbide-forming element. However, little attention has been paid to the effects of alloying elements on the pore-grain boundary separation behavior, which can help to achieve high densities, especially for 420 stainless steel systems.

This study examined the effects of C addition and the pre-alloyed Nb content on the sintering behavior of MIM 420 stainless steel. The evolution of density, grain size, and pore characteristics at different temperatures was investigated. Theoretical calculations were carried out to analyze the pore-grain boundary separation behavior during sintering. The results reported in this paper provide theoretical guidance for the large scale production of MIM stainless steel.

2. Experimental Methods

In this study, 420 stainless steel, 420Nb pre-alloyed, and graphite powders provided by Hunan Hengji Technology Ltd. (Yueyang, China) were used. The compositions and particle sizes of the stainless steel powders are listed in Table 1, and the powder morphology is shown in Figure 1.

Table 1. Element content of different raw material powders.

Element	Cr	Nb	Si	Mn	C	O	N	Fe	D_{50}/μm
Standard	12–14	-	≤1	≤1	0.16–0.25	-	-	Bal.	-
420	12.3	-	0.35	0.78	0.29	0.079	0.13	Bal.	13.1
420Nb	12.5	2.87	0.30	0.63	0.38	0.069	0.14	Bal.	12.49

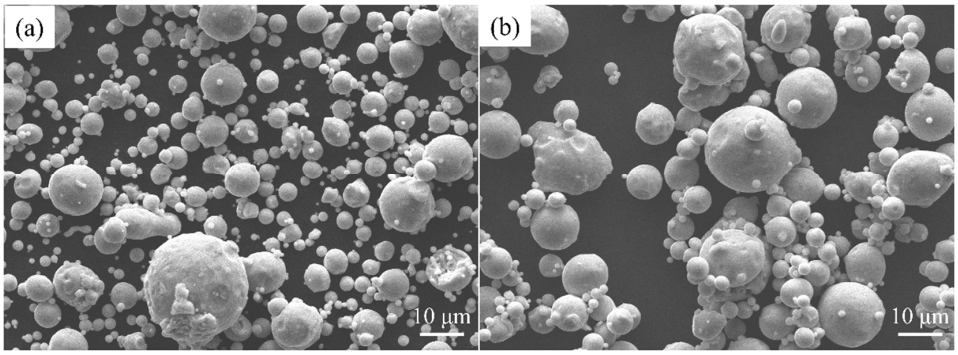

Figure 1. Scanning electron microscopy (SEM) images of the stainless steel powder (**a**) 420 and (**b**) 420Nb.

The stainless steel powder was mixed with a paraffin wax-based binder with a total powder loading of 58% in a rubber mixer at 150 °C for 120 min. The feedstock was injected into a cylinder mold of Ø 6 × 8 mm. A two-step debinding method consisting of catalytic debinding and thermal debinding was used to remove the binder. Catalytic debinding was performed using nitric acid as the catalyst at 110 °C for 8 h. The highest thermal debinding temperature was 900 °C, and the holding time was 1 h. The as-debound specimens were sintered at 1330, 1350, and 1370 °C. The holding time ranged from 15 to 240 min. A VQS-113 high-temperature vacuum-sintering (CENTORR Inc., Nashua, NH, USA) furnace was adopted with a vacuum of 0.1 Pa, and the temperature error was ±2.5 °C.

The densities of the sintered parts were measured by the Archimedes method, and the samples with open pores were sealed with wax. At least three samples were measured to obtain the average value for each sintering condition. The porosities and grain sizes of the as-sintered specimens were observed by a Leica metallographic microscope (LINKAM Inc., Wetzlar, Germany). The microstructure was observed by a JSM-6360 scanning electron microscope (JOEL Inc., Tokyo, Japan).

3. Results and Discussion

3.1. Density

Figure 2 shows the relative densities of specimens sintered at different temperatures. The density tends to increase with the increase of the sintering temperature and sintering time. The density of each sample increases at a relatively high rate from 0–1 h, and thereafter the rate of increase decreases. At 1330 °C, the densities of all specimens are approximately 90% or even lower to 77%. Carbon promotes sintering at 0–1 h and then the density of 420 catches up with that of 420 + 0.3C at 2–4 h. Among all the samples analyzed, 420Nb shows the lowest density at all times. It can be concluded that while C promotes sintering in the initial stage at low temperatures, Nb hinders the densification rate. At 1350 °C, the trend in the first hour is similar to that at 1330 °C. After 2 h, the densification rates of 420 and 420 + 0.3C slow down, and the latter is lower than the former. Conversely, the densification rate of 420Nb continues to rise, reaching 94.66% after 4 h, which is much higher than those of the other two samples (approximately 92%). Thus, at higher temperatures, Nb shows a beneficial effect on the densification, while the effect of carbon is debatable. At 1370 °C, the density of samples with C increases sharply from 0–2 h, followed by 420Nb, and 420 shows the lowest density among all the samples.

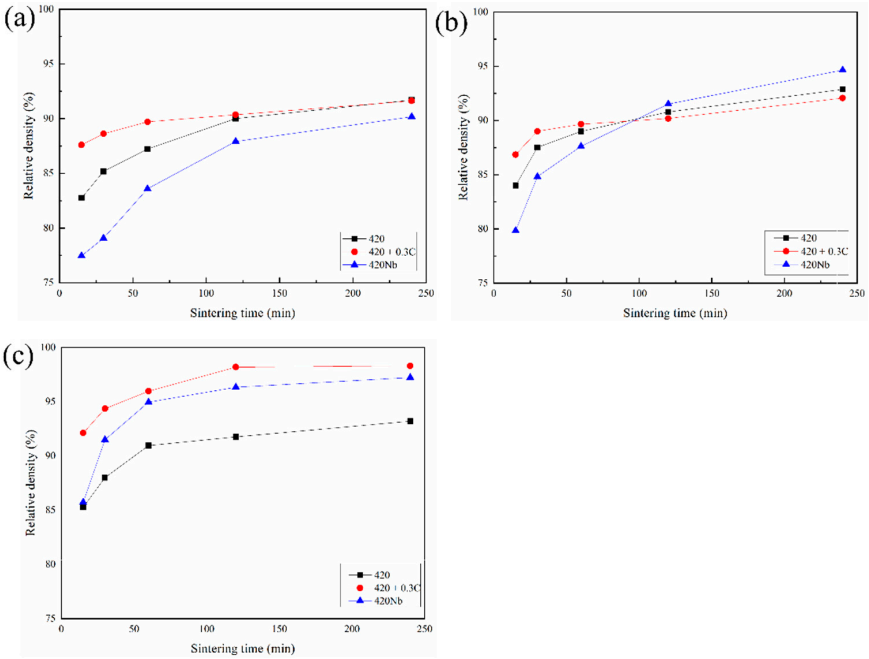

Figure 2. Relative density of MIM 420 specimens sintered at different temperatures: (**a**) 1330 °C; (**b**) 1350 °C; (**c**) 1370 °C.

3.2. Microstructure

Figure 3 shows the microstructure of specimens sintered at 1370 °C. The grain size of 420 + 0.3C grows rapidly, followed by 420, while the growth rate of 420+Nb is not obvious. Figure 4 shows the SEM images of the samples sintered at 1370 °C for 4 h. A large number of closed pores is observed inside the grains, which indicates that considerable pore-grain boundary separation has taken place. It can be seen from Figure 4d that the pores in the 420 + 0.3C sample are spheroidized with large diameters, whereas the 420 sample is partially spheroidized, and the pore spheroidization of the 420Nb sample is vague. The white spots in Figure 4f correspond to NbC precipitates. In 420Nb specimens shown in Figure 4g, the liquid phase appears along the grain boundaries; this was not observed in specimens sintered under other conditions.

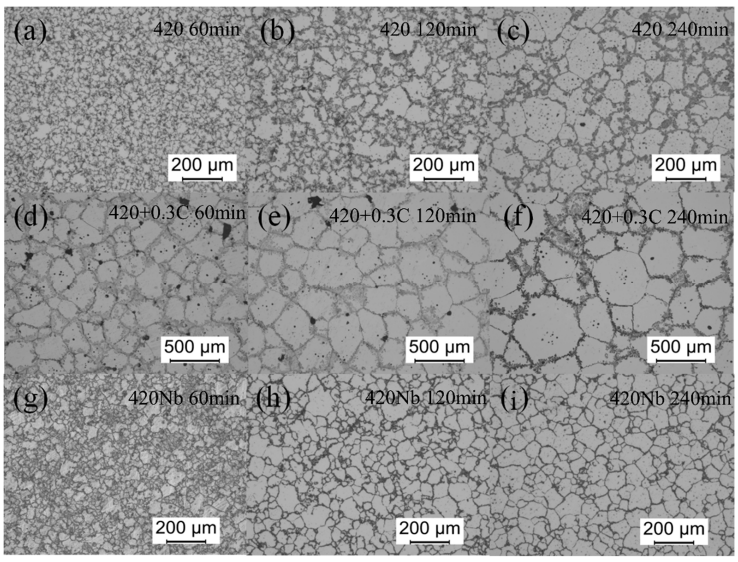

Figure 3. Microstructure of specimens sintered at 1370 °C: (**a**) 420, 60 min; (**b**) 420, 120 min; (**c**) 420, 240 min; (**d**) 420 + 0.3C, 60 min; (**e**) 420 + 0.3C, 120 min; (**f**) 420 + 0.3C, 240 min; (**g**) 420Nb, 60 min; (**h**) 420Nb, 120 min; (**i**) 420Nb, 240 min.

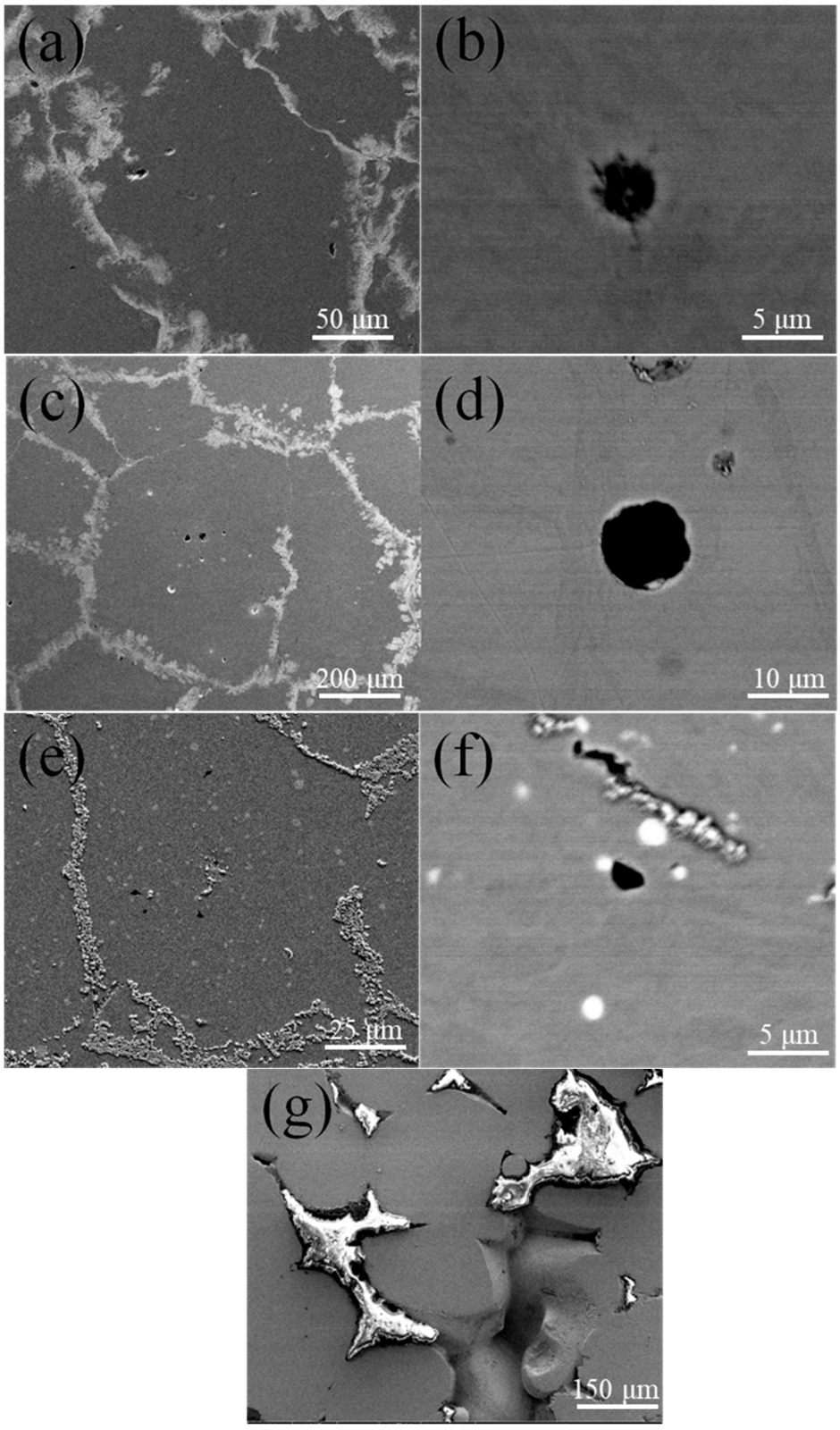

Figure 4. SEM images of specimens sintered at 1370 °C: (**a**,**b**) 420; (**c**,**d**) 420 + 0.3C; (**e**,**f**) 420Nb; (**g**) liquid phase characteristics in 420 + 0.3C.

The dependencies of the grain sizes are shown in Figure 5. As the sintering progresses, the grains grow significantly when the density increases to values above 90%. The growth rate of the 420Nb sample is the slowest, followed by the 420. The growth rate of 420 + 0.3C

is much higher than those of the other two samples. In the early stage of sintering (0–1 h), the sintering rate of samples with C increased significantly. The main reason for this is that C can reduce the concentrations of surface oxides, such as Fe_2O_3 and Cr_2O_3, thereby reducing the energy required for Fe atom transition and promoting the formation of sintering necks [24,25]. Concurrently, because of the decrease in the number of diffusion channels available for the diffusion of metallic atoms on the particle surface, the energy required for diffusion increases [26]. Nb atoms dissolved in steel combine with C to form NbC (thermodynamically proven to dissolve at ~1460 °C) and reduce the diffusion rate of C, thereby hindering C from reducing the surface oxides at low temperatures, which decreases the sintering rate.

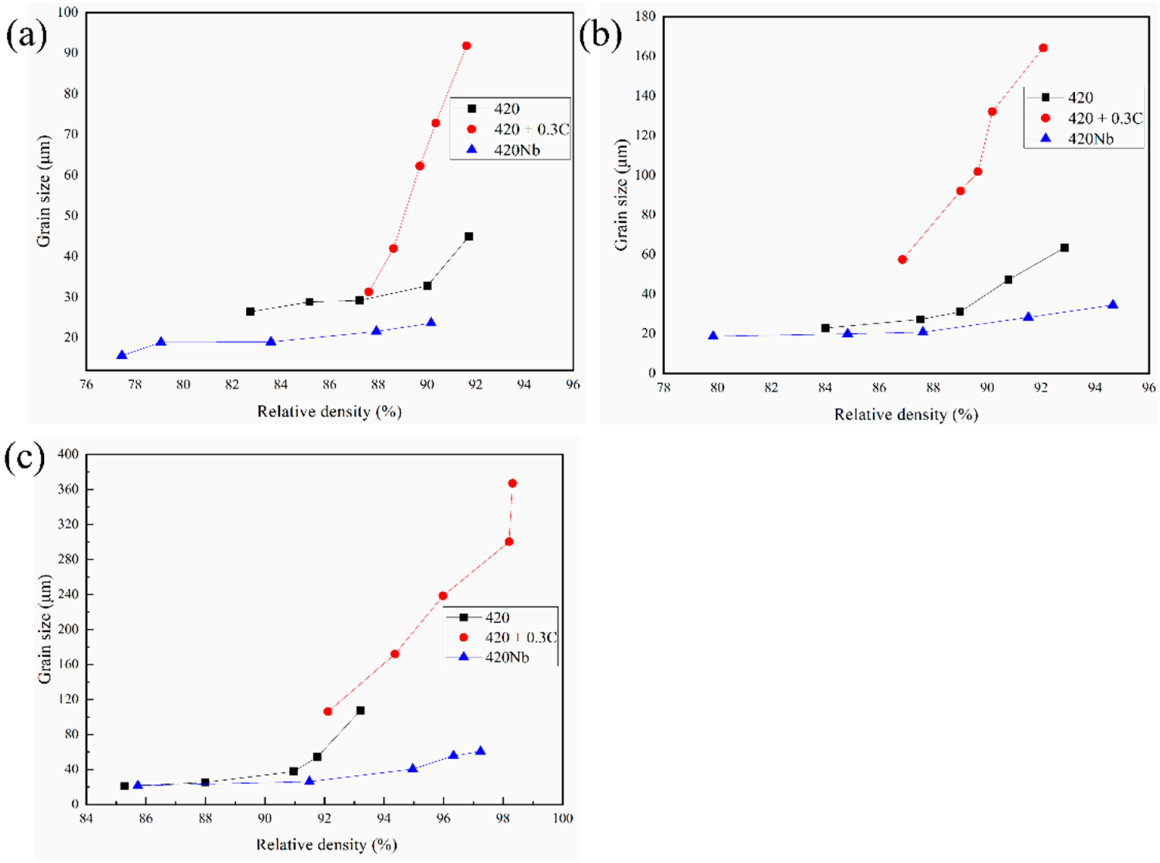

Figure 5. Grain size versus relative density curves of specimens sintered at different temperatures. (**a**) 1330 °C; (**b**) 1350 °C; (**c**) 1370 °C.

When the sintering progresses to the intermediate and final stages (1–4 h), grain boundary diffusion becomes the major mechanism for mass transport. The pores around the grain boundary is largely eliminated by the grain boundary diffusion, and the density of the material is improved. However, an excessively fast grain growth rate causes the grain boundaries to separate from the pores, and the grain boundary pores become closed pores, which are difficult to eliminate by solid phase sintering; thus, the increase in densities is retarded [27–29]. This phenomenon is evident in 420 stainless steel, and even more profound in 420 + 0.3C (below 1350 °C). Solid-dissolved C atoms can increase the self-diffusion ability of Fe atoms and thereby promote grain growth. The phenomenon of the grain boundary-pore separation is obvious when the grain size increases at highest speed. Thus, 420 + 0.3C shows the lowest density at 1350 °C. However, Nb inhibited the diffusion of carbon. Moreover, NbC dispersed in the matrix can hinder the movement of the grain boundaries, thus inhibiting the growth of the grain size of the material. The slow growth rate of the grains prolongs the transit time of pore vacancies along the grain boundaries. Therefore, 420Nb shows the highest density at 1350 °C.

The highest density for 420 + 0.3C is observed for specimens sintered at 1370 °C. This is mainly because of the generation of a liquid phase. In general, the temperature at which the liquid phase appears in the material is approximately 1385 °C. The formation of a liquid phase at 1370 °C may be due to the high concentration of the local carbon in the material, which facilitates a eutectic liquid phase. The density increases rapidly because the liquid phase can rearrange the powder particles and accelerate the atomic diffusion through the liquid phase [30,31]. The liquidus temperature points of 420 and 420Nb are 1420 °C and 1405 °C, respectively. Since they are pre-alloyed powders, the possible presence of a eutectic liquid phase is irrelevant.

3.3. Pore and Grain Boundary Interaction

In the later stages of sintering, the grain boundary area per unit volume (S_V) is a linear function of the interfacial pore area per unit volume (S_{VP}); this has been previously demonstrated in Nb, Cu, and W systems [9–11]. The S_V is calculated from the stereo relationship $S_V = 2/k$, where k is the grain size [9]. The values of S_{VP} represent the porosity of the sintered sample. By fitting the data in Figure 5, the relationship between S_V and S_{VP} can be determined as shown in Figure 6. The images indicate that S_{VP} is proportional to S_V, and the slopes of the S_V versus S_{VP} curves are different for various samples.

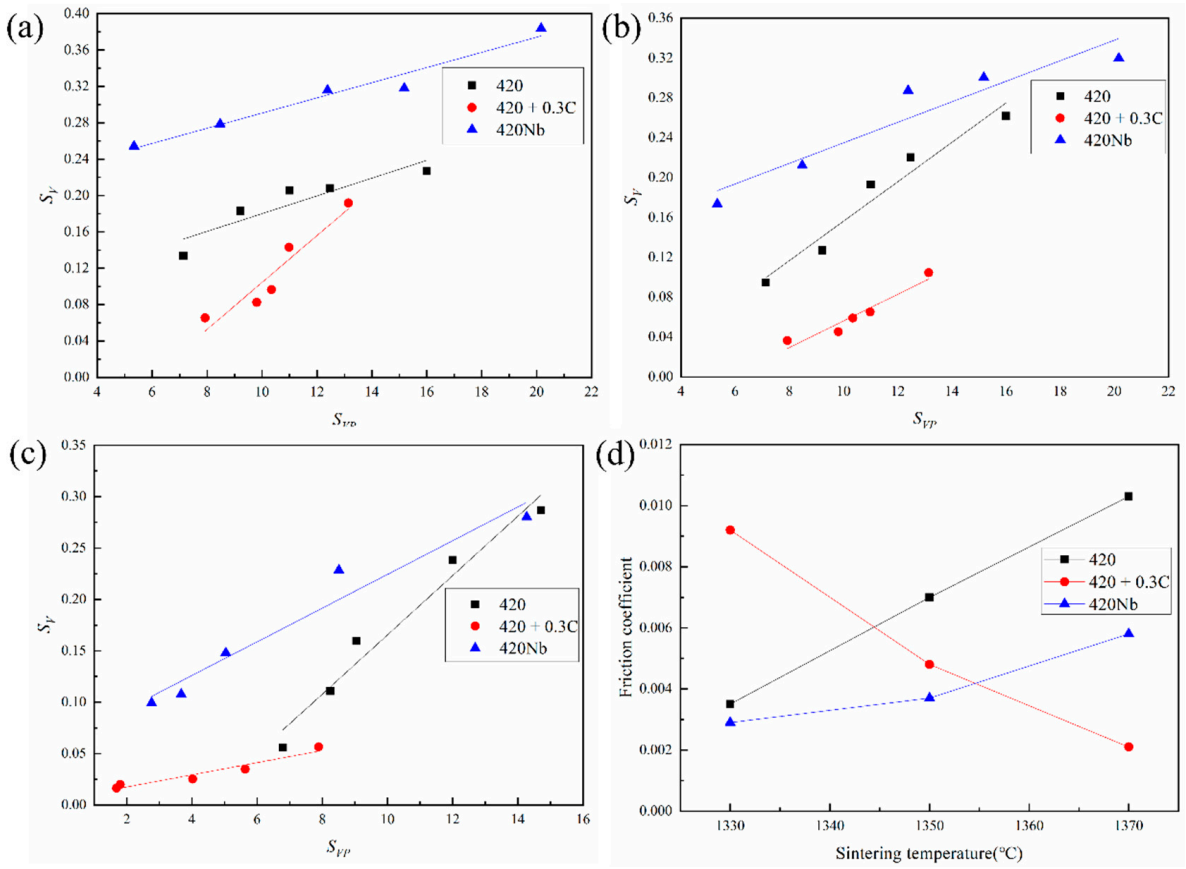

Figure 6. Trend of grain boundary area per unit volume (S_V) with the pore area per unit volume (S_{Vp}) at different temperatures: 1330 °C; (**a**) 1330°C, (**b**) 1350 °C; (**c**) 1370 °C and (**d**) friction coefficient.

The interaction between pores and grain boundaries is similar to friction force. The relationship between the S_V and S_{VP} is [9]:

$$S_V = 3\mu\gamma_P S_{VP}/\gamma \quad (1)$$

where μ is a dimensionless friction coefficient, γ_p is the pore energy per unit area, and γ is the grain boundary energy per unit area.

The surface energy of the pores is replaced by the surface energy of the material [9], and the grain boundary energy (2.13 J/m^2) [32] and surface energy (2.42 J/m^2) [33] of the material are substituted into the Formula (1), both of which are material-dependent constants. The relationship between the μ values of different samples at three temperatures is shown in Figure 6d; the friction coefficients of the 420 and 420Nb samples increase with an increase in temperature (i.e., a positive slope), whereas the slope of 420 + 0.3C is negative.

During the sintering process, S_V and S_{VP} maintained a good linear relationship under the different porosities of the three samples, which indicates that the interaction between pores and grain boundaries is independent of the porosity and is related to the alloy composition and temperature. A previous study has found that the binding energy is a key factor affecting the friction coefficient between grain boundaries and pores and is directly proportional to the friction coefficient, which is consistent with the results for HK30 steel reported by He [6]. As the sintering process progresses, the density of the materials increases; thus, the binding energy of the material as well as the friction coefficient increase. For the 420 + 0.3C sample, the liquid phase formed at high temperatures deceases the friction coefficient. However, the friction coefficients of the 420 + 0.3C samples is much larger than those of 420 and 420Nb samples at 1330 °C, which is probably because the pores in the 420 + 0.3C samples are much larger in size, and the large pores need more time to break away from the grain boundaries; however, this needs to be verified through subsequent experiments. Image-Pro was used to measure the pore size of the samples in the SEM image of more than 1 μm, and 40 pores of each sample were examined. The average pore sizes of 420 + 0.3C, 420, and 420Nb samples sintered at 1370 °C for 4 h are 13.45, 4.75, and 2.72 μm, respectively. This indicates that it is more difficult to separate the grain boundary of the 420 sample from the pores compared to the others, and hence the friction coefficient of 420 is larger than that of 420Nb.

3.4. End Point of Sintering

At 1330 °C, the increase in density is negligible after holding for 2 h, and the relative density is approximately 91% for 420 and 420 + 0.3C. At 1350 °C, the sintering rate after 2 h is also very slow. From Figure 5c, only the grain size increases in the later stage of sintering at 1370 °C, while the density remains stable. Thus, there exists an end point of sintering, after which the densification rate is very slow, but the grain growth rate is very fast.

Here we propose a model to predict the probability of contact between pores and the grain boundary, which aids in predicting the end point of sintering, as shown in Figure 7. It is assumed that the porosity is a constant (assumed to be 5%) and that the pores are randomly and uniformly distributed. The grains and the pores are spherical in shape, with radii of R and r, respectively. Thus, the grain boundary is completely separated from the pores when the pore-sphere-center is located in the region of $0 \approx R - r$, as shown in Figure 7b. When the pore center is located in the region of $R - r \approx R$, the grain boundary intersects with the pores, and the pores can also be eliminated by grain boundary diffusion, as shown in Figure 7a. The probability of the pore sphere center falling in the $R - r \approx R$ region and the total number of contact pores in 1 mm^3 can be calculated by the following formulas:

$$N = \frac{R^3 - (R - r)^3}{R^3} \tag{2}$$

$$M = N \times n \times m \tag{3}$$

where N is the probability of the pore sphere center being situated in the $R - r \approx R$ region. The higher the probability, the easier is the sintering process. M is the number of pores in contact with the grain boundary in 1 mm^3, n represents the number of grains in 1 mm^3, and m represents the number of pores contained in a grain.

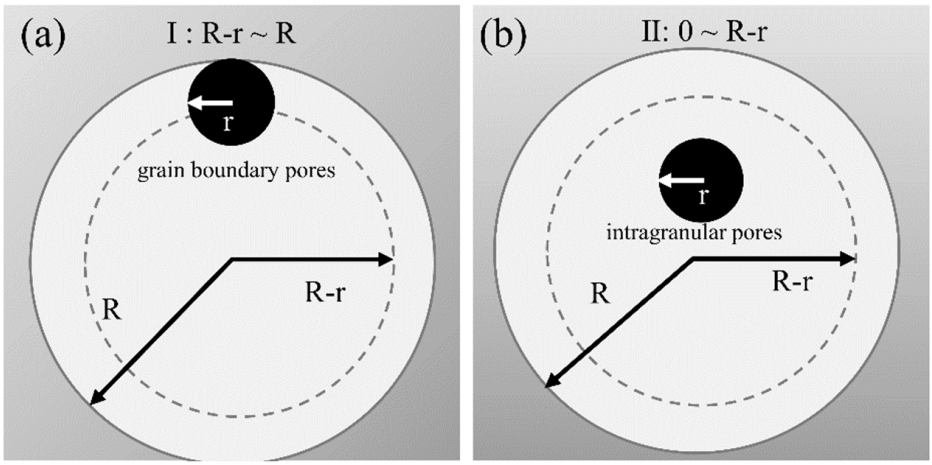

Figure 7. Schematic diagram of the pore-grain boundary separation model. (**a**) the grain boundary intersects with the pores, (**b**) the grain boundary is completely separated from the pores.

The results calculated by fitting the data for 420, 420 + 0.3C, and 420Nb into Formulas (2) and (3) are shown in Figure 8a. When the pore size is fixed, the larger the grain size, the smaller the contact probability between the pores and the grain boundary, and in turn the slower the densification rate. When the grain size is very small, an increase in grain size significantly reduces the contact probability. However, when the grains grow to a certain degree and the probability of contact between the pores and the grain boundaries is approximately 10%, the downward trend of the contact probability begins to plateau. At this point, the grain size to pore size ratio is ~28. The grain growth rate increases thereafter. The extremely low probability of pore contacts also causes the sintering to stagnate. It can be observed from the figure that the last solid point (1370 °C, 4 h) in the figure is close to this ratio, while 420Nb is higher than 10% (N = 12.8%). This explains why the density of 420Nb increases from 2 h to 4 h, while the improvement of 420 + 0.3C is very tiny, as shown in Figure 2c. Figure 8b shows the relationship between the number of pores in contact with the grain boundaries and the grain size in a volume of 1 mm^3. Although there are opportunities for large holes to contact the grain boundaries, the number of pores in contact is small. Large pores require more time to eliminate, and thus, among the materials analyzed in this study, even at the same R/r ratio, 420 + 0.3C is the most difficult to densify, while 420Nb is the easiest.

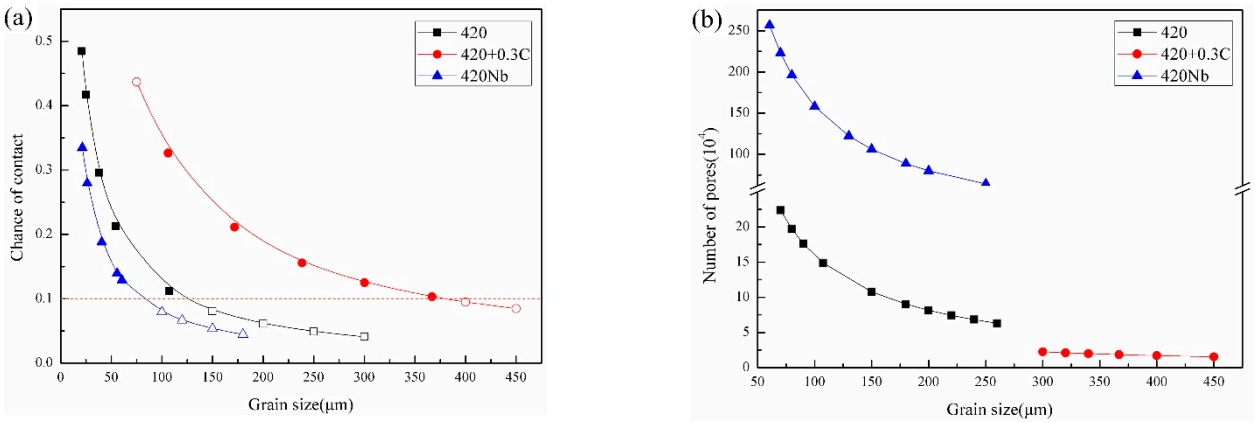

Figure 8. Relationship between pores in contact with grain boundaries and the grain size: (**a**) probability of contact and (**b**) quantity (solid points refer to the data obtained in the experiment, and dotted points refers to the estimated value).

4. Conclusions

1. C promotes the surface oxide reduction to accelerate the sintering process at low temperatures, and thus the strong carbide-forming element Nb inhibits the early sintering of 420. The addition of C accelerates the pore-grain boundary separation at 1350 °C and prevents (or at least retards) the diffusion of the grain boundaries. In contrast, Nb suppresses the rate of grain boundary movement and promotes densification from 1350 °C onward.
2. C accelerates the speed of grain boundary movement and promotes the growth of grains, which reach the size of 367 μm after sintering at 1370 °C for 4 h. Nb combines with C to form NbC, which can inhibit the grain growth. The grain size is 60 μm when sintered at 1370 °C for 4 h.
3. The S_V exhibits a good linear relationship with S_{VP} and is related to the chemical composition and temperature, rather than to the porosity.
4. When the ratio of grain size to pore size is 28, the probability of contact between pores and grain boundaries is only 10%. The sintering rate is slow, and the grain growth is fast, which is consistent with the experimental results.

Author Contributions: T.W.: data curation, writing—original draft, investigation. H.H.: conceptualization, writing—review and editing, funding acquisition, supervision. J.L.: conceptualization, funding acquisition, project administration, writing—review and editing, supervision. M.G.: investigation. X.L.: investigation. Y.H.: investigation. W.X.: conceptualization, investigation, funding acquisition. All authors have read and agreed to the published version of the manuscript.

Funding: This research was funded by National Natural Science Foundation of China (52164042 and 51804271); Scientific Research Foundation of Hunan Provincial Education Department (21B0121). The Guangdong Academy of Sciences Project of Science and Technology Development (2020GDASYL-20200103109). Guangdong Basic and Applied Basic Research Foundation (2019A1515110710 and 2021A1515012086).

Institutional Review Board Statement: Not applicable.

Informed Consent Statement: Not applicable.

Data Availability Statement: Not applicable.

Conflicts of Interest: The authors declare no conflict of interest. The authors declare that they have no known competing financial interests or personal relationships that could have appeared to influence the work reported in this paper.

References

1. Xi, Y.T.; Liu, D.X.; Han, D. Improvement of corrosion and wear resistances of AISI 420 martensitic stainless steel using plasma nitriding at low temperature. *Surf. Coat. Technol.* **2008**, *202*, 2577–2583. [CrossRef]
2. Zhang, Z.; Farahmand, P.; Kovacevic, R. Laser cladding of 420 stainless steel with molybdenum on mild steel A36 by a high power direct diode laser. *Mater. Des.* **2016**, *109*, 686–699. [CrossRef]
3. Attia, U.M.; Alcock, J.R. A review of micro-powder injection moulding as a microfabrication technique. *J. Micromech. Microeng.* **2011**, *21*, 043001. [CrossRef]
4. Lou, J.; Li, Y.M.; He, H.; Li, L.J. Effect of atomisation medium on sintering properties of austenitic stainless steel by eliminating influence of particle shape and particle size. *Powder Metall.* **2010**, *53*, 112–117. [CrossRef]
5. An, C.F.; He, H.; Li, Y.M.; Yin, J.; Lou, J.; Yu, Y. Effects of C and Nb addition on the structure and properties of 420 stainless steel in metal injection molding. *J. Guangxi Univ. Sci. Technol.* **2018**, *29*, 63–69.
6. Hu, Y.H.; Li, Y.M.; Lou, J.; He, H.; Zhang, X. Effects of Sintering Temperature and Holding Time on Densification and Mechanical Properties of MIM HK30 Stainless Steel. *Int. J. Metall. Met. Phys.* **2018**, *3*, 22.
7. Ertugrul, O.; Park, H.S.; Onel, K.; Porada, M.W. Effect of particle size and heating rate in microwave sintering of 316L stainless steel. *Powder Technol.* **2014**, *253*, 703–709. [CrossRef]
8. Patterson, B.R.; Liu, Y.; Griffin, J.A. Degree of Pore-Grain-Boundary Contact During Sintering. *Metall. Mater. Trans. A* **1990**, *21*, 2137–2139. [CrossRef]
9. Zilnyk, K.D.; Leite, G.S.; Sandim, H.R.Z.; Rios, P.R. Grain growth inhibition by connected porosity in sintered niobium. *Acta Mater.* **2013**, *61*, 5821–5828. [CrossRef]

10. Aigeltinger, E.H.; Exner, H.E. Stereological characterization of the interaction between interfaces and its application to the sintering process. *Metall. Trans. A* **1977**, *8*, 421–424. [CrossRef]
11. Ting, C.J.; Lu, H.Y. Defect reactions and the controlling mechanism in the sintering of magnesium aluminate spinel. *J. Am. Ceram. Soc.* **1999**, *82*, 841–848. [CrossRef]
12. Guo, S.; Wang, H.; Xu, P. Effect of pretreated microstructure on subsequent sintering performance of $MgAl_2O_4$ ceramics. *Ceram. Int.* **2019**, *45*, 7544–7551. [CrossRef]
13. Cabral Miramontes, J.A.; Barceinas Sánchez, J.D.O.; Almeraya Calderón, F.; Martinez Villafañe, A.; Chacón, J.G. Effect of Boron Additions on Sintering and Densification of a Ferritic Stainless Steel. *J. Mater. Eng. Perform.* **2010**, *19*, 880–884. [CrossRef]
14. Simchi, A. Effect of C and Cu addition on the densification and microstructure of iron powder in direct laser sintering process. *Mater. Lett.* **2008**, *62*, 2840–2843. [CrossRef]
15. Sun, L.; Kim, Y.H.; Kim, D. Densification and properties of 420 stainless steel produced by three-dimensional printing with addition of Si3N4 powder. *J. Manuf. Sci. Eng.* **2009**, *131*, 061001. [CrossRef]
16. Chen, C.; Duan, C.; Li, Y. Effects of Cu content on the microstructures and properties of Cr–Cu composite coatings fabricated via mechanical alloying method. *Powder Technol.* **2015**, *277*, 36–46. [CrossRef]
17. Lou, J.; He, H.; Li, Y.M.; Zhang, H.; Fang, Z.; Wei, X. Effects of Trace Carbon Contents on Lattice Distortion and Nano-Copper Phase Precipitation in Metal Injection-Molded 17-4PH Stainless Steel. *JOM* **2019**, *71*, 1073–1081. [CrossRef]
18. Giménez, S.; Zubizarreta, C.; Trabadelo, V. Sintering behaviour and microstructure development of T42 powder metallurgy high speed steel under different processing conditions. *Mater. Sci. Eng. A* **2008**, *480*, 130–137. [CrossRef]
19. Zhang, H.; He, H.; Li, Y.M. Effect of carbon content on microstructure and mechanical properties of metal injection molded HK30 stainless steel. *Powder Metall.* **2017**, *22*, 739–746.
20. Harun, W.; Toda, K.; Osada, T. Effect of MIM Processing Parameters on the Properties of 440C Stainless Steel. *J. Jpn. Soc. Powder Powder Metall.* **2012**, *59*, 264–271. [CrossRef]
21. Jiang, F. Study on the Influence of Alloy Elements on the Properties and Structure of Powder Metallurgy Low Alloy Steel. Master's Thesis, Central South University, Changsha, China, 2004.
22. Zhang, L.; Li, Z.Y.; Zhou, K.C. Effect of elemental powder prealloying on microstructure and properties of sintered alloy steel. *Powder Metall. Mater. Sci. Eng.* **2005**, *10*, 34–39.
23. Zhuang, K.X.; Huang, K.X. Prediction and demonstration of sintering window of alloy element and carbide super solid phase liquid phase sintered stainless steel. In Proceedings of the 2011 National Conference on Powder Metallurgy and Symposium on Powder Metallurgy across the Taiwan Straits, Taipei, Taiwan, 8–15 December 2011.
24. An, P.L.; Song, L.L.; Hang, W.; Chen, H.Z. Characterization of oxide on the water atomised FeMn powder surface. *Appl. Surf. Sci.* **2014**, *295*, 180–188.
25. Hryha, E.; Gierl, C.; Nyborg, L.; Danninger, H.; Dudrova, E. Surface composition of the steel powders pre-alloyed with manganese. *Appl. Surf. Sci.* **2010**, *256*, 3946–3961. [CrossRef]
26. He, H.; Lou, J.; Li, Y.M. Effects of oxygen contents on sintering mechanism and sintering-neck growth behaviour of FeCr powder. *Powder Technol.* **2018**, *329*, 12–18. [CrossRef]
27. Hsueh, C.H.; Evans, A.G.; Coble, R.L. Microstructure development during final/intermediate stage sintering—I. Pore/grain boundary separation. *Acta Metall.* **1982**, *30*, 1269–1279. [CrossRef]
28. Sakarcan, M.; Hsueh, C.H.; Evans, A.G. Experimental Assessment of Pore Breakaway During Sintering. *J. Am. Ceram. Soc.* **2010**, *66*, 456–461. [CrossRef]
29. Djohari, H.; Derby, J.J. Transport mechanisms and densification during sintering: II. Grain boundaries. *Chem. Eng. Sci.* **2009**, *64*, 3810–3816. [CrossRef]
30. German, R.M. *Liquid Phase Sintering*; Plenum Press: New York, NY, USA, 1985.
31. German, R.M.; Suri, P.; Park, S.J. Review: Liquid phase sintering. *J. Mater. Sci.* **2009**, *44*, 1–39. [CrossRef]
32. Wang, Y.M.; Peng, F. Energy calculation of Fe (001) twist grain boundary. *J. Shangqiu Teach. Coll.* **2009**, *25*, 63–68.
33. Vitos, L.; Ruban, A.V.; Skriver, H.L.; Kollár, J. The surface energy of metals. *Surf. Sci.* **1998**, *411*, 186–202. [CrossRef]